

# Calculations of Hydrogen Associative Desorption on Mono- and Bimetallic Catalysts

Huiling Zheng,<sup>||</sup> Hao Li,<sup>||</sup> Weiyu Song, Zhen Zhao,<sup>\*</sup> and Graeme Henkelman<sup>\*</sup>

Cite This: *J. Phys. Chem. C* 2021, 125, 12028–12037

Read Online

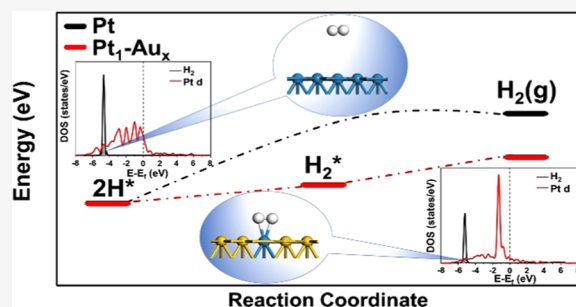
ACCESS |

Metrics & More

Article Recommendations

Supporting Information

**ABSTRACT:** Transition-metal-based materials can activate C–H and O–H bonds in industrially significant reactions such as hydrocarbon and alcohol reforming. Recently, bimetallic alloys based on Au, Ag, and Cu have shown unique chemistry including coke-resistance, promising reaction activity, and interesting product selectivity. However, the mechanism of their key reaction step, the hydrogen associative desorption process, is not well-understood. In this work, density functional theory calculations were used to study the kinetics and thermodynamics of hydrogen associative desorption on 8 monometallic and 70 bimetallic Au–, Ag–, and Cu–X (X = Ir, Ni, Pd, Pt, and Rh) close-packed surfaces. We identified two different mechanisms for hydrogen associative desorption on these surfaces, which are selected by the density of states overlap between a gas-phase H<sub>2</sub> molecule and the d-band of the surface metal. We show that specific bimetallic atomic ensembles have significantly lower kinetic barriers for hydrogen associative desorption. A linear correlation between the hydrogen desorption barriers and the reaction energies was found for most of the surfaces studied. More importantly, we show that a Au-/Ag-/Cu-rich ensemble alloy with a small portion of a strong-binding metal can effectively lower the hydrogen associative desorption barrier. This finding is significant for the design of highly active and selective catalysts for H<sub>2</sub> production through the activation of organic molecules.



## 1. INTRODUCTION

Transition-metal-based materials are known to activate the C–H, O–H, C–C, and C–O bonds for many reactions.<sup>1,2</sup> In particular, Ni, Ru, Rh, Pd, Pt, and Ir have been shown to be effective for CH<sub>4</sub> dissociation, CH<sub>4</sub>–CO<sub>2</sub> reforming, ethanol reforming, and glycerol reforming.<sup>3–12</sup> Ni is one of the most widely used catalysts for this application due to its low cost and high activity. However, carbon deposition can easily occur on Ni surfaces, resulting in the deactivation of the catalyst.<sup>4,8,13–17</sup> Compared to Ni-based catalysts, noble metals such as Rh, Ru, Pd, Pt, and Ir are less sensitive but also suffer from carbon deposition and are much more expensive.<sup>4,8,17–19</sup>

Hydrogen associative desorption is a proven key step for these C–H and O–H activation reactions from both experimental and theoretical studies,<sup>10,20,21</sup> which significantly affect the reaction activity, selectivity, and hydrogen production and storage. However, due to the strong adsorption capacity, Ni, Rh, Pt, Ru, Pd, and Ir are not facile for the hydrogen associative desorption process.<sup>22–28</sup> Some bimetallic alloys have been demonstrated as promising alternatives that improve the reaction activity with less coking. For example, Ni-based bimetallic catalysts were studied using both experiments and density functional theory (DFT) calculations, showing better catalytic activity and less coke formation, including Ni–Au,<sup>29,30</sup> Ni–Ag,<sup>31</sup> Ni–Cu,<sup>13</sup> Ni–Pt,<sup>32–34</sup> Ni–Pd,<sup>33</sup> and Ni–Rh.<sup>35</sup> Pd–Au has been widely reported as a stable catalyst with promising activity for H<sub>2</sub> production;<sup>36–38</sup> the active Pd

ensembles on a Au surface are able to make hydrogen desorption more facile after C–H and O–H activation.<sup>10</sup> Ag–Pd core–shell catalysts have been reported as active for H<sub>2</sub> production from HCOOH decomposition at room temperature, achieving ~100% conversion of HCOOH with a high selectivity toward CO<sub>2</sub> formation.<sup>39</sup> The strong Ag–Pd ligand effect originating from charge transfer to the Pd surface significantly reduces the binding strengths of HCOO\* and HCO\*, which enhances H<sub>2</sub> production selectivity.<sup>40</sup> In addition, our recent combined theoretical and experimental studies have shown that the ensemble effect (specific geometries of an alloy reaction site)<sup>41,42</sup> can significantly affect the alcohol decomposition activity and H<sub>2</sub> production on bimetallic catalysts. Specifically, different sizes of Pd ensembles on Au(111) can affect the mechanism of ethanol dehydrogenation and H<sub>2</sub> production, showing a dependence of the initial dehydrogenation selectivity of ethanol on the size of Pd ensembles.<sup>10,43</sup> A similar conclusion was found for Rh–Au alloys.<sup>44</sup> In addition, different ensemble geometries on

Received: April 17, 2021

Revised: May 13, 2021

Published: May 26, 2021



PtAu(111) surfaces have shown a significant impact on the performance of HCOOH oxidation.<sup>45</sup>

Compared to those strong-binding transition metals, Au, Ag, and Cu are known to be less active for C–H/O–H activation and H<sub>2</sub> dissociation due to their inert electronic structures.<sup>46,47</sup> Therefore, combinations of Au, Ag, or Cu with highly effective bond-activation (*i.e.*, the strong-binding) metals (*i.e.*, Ni, Rh, Pd, Pt, or Ir) are expected to show higher catalytic activity due to coking resistance and more facile hydrogen desorption. Analyzing hydrogen associative desorption on these bimetallic alloys can help identify high-performing catalysts to facilitate organic molecule reforming and H<sub>2</sub> production, which ultimately provides rational guidelines for the design of promising hydrogen storage and fuel cell materials.

Based on the reasons above, we are motivated to study hydrogen associative desorption on 8 monometallic and 70 bimetallic close-packed surfaces. First, we identified two different mechanisms of hydrogen associative desorption on these surfaces: one with the formation of stabilized H<sub>2</sub>\* as the intermediate (denoted as Mechanism 1) and the other with the direct formation of gas-phase H<sub>2</sub> (denoted as Mechanism 2). DFT calculations were performed to determine both the kinetics and thermodynamics of hydrogen associative desorption on these surfaces as well as the corresponding mechanism for each site. We found that monometallics Au, Ag, Ir, and Pt and the bimetallic surfaces of Ir–Au, Ir–Ag, and Ir–Cu follow Mechanism 2 while monometallics Cu, Ni, Pd, Rh, and all other bimetallic catalysts follow Mechanism 1. We calculated the projected density of states (PDOS) of the gas-phase H<sub>2</sub> and the d-electrons of the surface metal atoms to understand the selectivity toward the two mechanisms. We further found that hydrogen desorption on these close-packed surfaces follows a linear Brønsted–Evans–Polanyi (BEP) relation, which indicates that one can directly predict the reaction kinetics with the reaction thermodynamics with minimal computational cost. The ensemble effect of these bimetallic alloys was also analyzed, from which we found that most of the bimetallic alloys with Au/Ag/Cu-rich ensembles can effectively reduce the energy barriers for hydrogen desorption.

## 2. COMPUTATIONAL AND MODELING METHODS

The Vienna Ab initio Simulation Package (VASP)<sup>48,49</sup> was used for the DFT calculations with the electron exchange–correlation effect described by the Perdew–Burke–Ernzerh functional within the generalized gradient approximation (GGA-PBE).<sup>50</sup> Spin polarization was tested and used as needed, including calculations of Ni(111) and Ni-based alloy surfaces. The projected augmented wave framework was used to describe the core–valence electron interaction.<sup>51</sup> A plane-wave basis set with an energy cutoff of 400 eV<sup>52</sup> was used to describe the valence electrons. A climbing image nudged elastic band (CI-NEB) method<sup>53,54</sup> was employed to locate transition states. All calculations were modeled on the (111) surface of a 4-layer (4 × 4) slab with the bottom two atomic layers fixed in bulk positions. This means the coverage of H<sub>2</sub> and co-adsorbed H considered in our calculations are 1/16 and 1/8, respectively. Calculations with thicker slabs were tested in our previous studies,<sup>21,22</sup> no significant differences were found for the adsorbate binding energies and geometries. Geometries were considered relaxed when the forces on each atom decreased below 0.05 eV/Å. A vacuum gap of at least 12 Å in the z-direction was used to separate periodic images. A

Monkhorst–Pack 3 × 3 × 1 *k*-point mesh was used for the Brillouin zone integration. For all of the key computational parameters, stricter settings were tested and showed a neglectable difference in the results. To model bimetallic alloys, we used strong-binding element X (X = Ir, Ni, Pd, Pt, and Rh) to substitute 1, 2 (2-fold), 3 (3-fold), 4 (4-fold), and 1 monolayer Au/Ag/Cu on the Au/Ag/Cu(111) surface. Several monolayer models including Ir<sub>m</sub>–Au<sub>x</sub>, Ir<sub>m</sub>–Ag<sub>x</sub>, Ni<sub>m</sub>–Au<sub>x</sub>, Ni<sub>m</sub>–Ag<sub>x</sub>, and Rh<sub>m</sub>–Au<sub>x</sub> did not converge to a commensurate configuration after optimization due to the large strain; these are not discussed further in this study. Since the synthesis of alloy catalysts is usually kinetically controlled (*i.e.*, microwave-assisted synthesis<sup>55</sup>), different types of ensembles can occur on an alloy surface even though some of them have relatively high formation energies. Therefore, we considered all of the possible compositions of each bimetallic triatomic ensemble.

The hydrogen (associative) desorption energies ( $E_{\text{des}}$ ) were calculated using the following equation

$$E_{\text{des}} = E_{\text{f}} - E_{\text{ini}} \quad (1)$$

where  $E_{\text{f}}$  and  $E_{\text{ini}}$  are the energies of the final and initial states of hydrogen associative desorption, respectively.

The hydrogen (dissociative) adsorption energies ( $E_{\text{ads}}$ ) were calculated using the following equation

$$E_{\text{ads}} = E_{\text{tot}} - E_{\text{slab}} - E_{\text{H}_2} \quad (2)$$

where  $E_{\text{tot}}$  is the total energy of the combined system with two isolated H atoms bound to the surface,  $E_{\text{slab}}$  is the energy of the bare slab, and  $E_{\text{H}_2}$  is the energy of an H<sub>2</sub> molecule in a vacuum. For comparison, we calculated the hydrogen desorption pathways on Pt and Pt–Au surfaces using the PBE, RPBE,<sup>56</sup> and PBE-D2<sup>57</sup> functionals, as shown in Table S1. We found that they all show similar mechanisms regardless of their desorption energy differences. In Jess Wellendorff's experimental benchmarking paper,<sup>58</sup> the errors in H<sub>2</sub> dissociative adsorption energies on single-crystal metals are the smallest with PBE as compared to other methods (RPBE, BEEF-vdW,<sup>59</sup> *etc.*). Therefore, PBE was used in this study.

## 3. RESULTS AND DISCUSSION

**3.1. Mechanism of Hydrogen Desorption.** For the process of hydrogen associative desorption from two co-

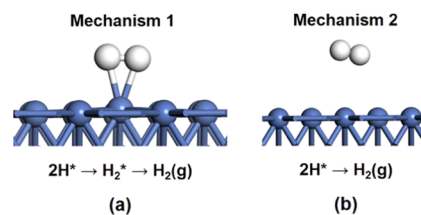


**Figure 1.** Two identified hydrogen associative desorption mechanisms on transition-metal surfaces. White and blue spheres represent H and the metal element, respectively.

adsorbed H\* atoms to a gas-phase H<sub>2</sub> molecule on monometallic surfaces (Au, Ag, Cu, Ir, Ni, Pd, Pt, and Rh(111)), there are two mechanisms as identified by the CI-NEB method. As shown in Figure 1a, Mechanism 1 first forms a stabilized H<sub>2</sub>\* adsorbed on the surface as an intermediate species, followed by the desorption of H<sub>2</sub>\*. In contrast, Mechanism 2 directly forms a gas-phase H<sub>2</sub> molecule on the surface (Figure 1b). Mechanism 1 is similar to a precursor

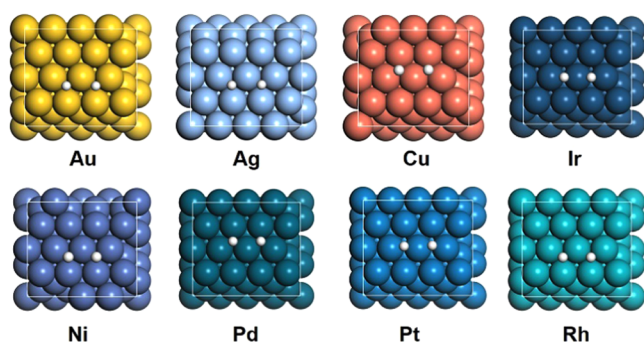


**Figure 2.** Initial states of hydrogen associative desorption with two co-adsorbed H\* atoms. Eight monometallic (111) surfaces (Au, Ag, Cu, Ir, Ni, Pd, Pt, and Rh) were considered in this study. Yellow, silver, red, deep blue, purple, deep green, blue, green, and white spheres represent Au, Ag, Cu, Ir, Ni, Pd, Pt, Rh, and H, respectively.

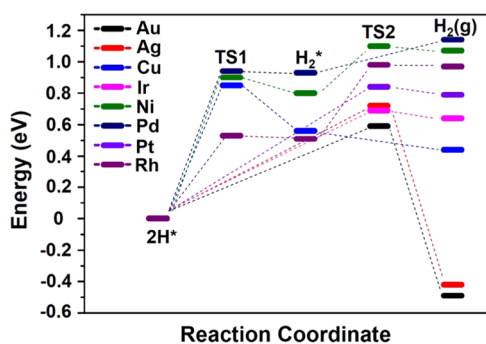


**Figure 3.** Free energy diagram of hydrogen desorption on monometallic (111) surfaces (Au, Ag, Cu, Ir, Ni, Pd, Pt, and Rh). TS represents the transition state located by the CI-NEB method.

mechanism for hydrogen dissociative adsorption in which H<sub>2</sub> molecule is temporarily trapped in a molecular physisorption state (the so-called precursor state)<sup>60,61</sup> before being dissociatively adsorbed.

The initial state of hydrogen desorption is with two co-adsorbed adjacent hydrogen atoms (Figure 2). We neglect modeling any H diffusion before desorption because H diffusion usually has a low diffusion barrier and is facile at

reaction temperatures.<sup>62</sup> There exist different adsorption sites (*i.e.*, bridge and hollow sites) for the most stable H\* co-adsorption at different monometallic surfaces. Co-adsorbed hydrogen atoms are preferably adsorbed on the hollow sites of Au, Ag, Cu, Ni, Pd, and Rh(111) while on the bridge sites of Ir and Pt(111) due to their broader 5d band.<sup>63,64</sup>

Figure 3 shows the free energy diagram of hydrogen desorption on eight monometallic surfaces, with the initial states shifted to zero. The hydrogen desorption pathways on the monometallic surfaces are shown in Figure S1. It can be seen that hydrogen desorption on Cu, Ni, Pd, and Rh(111) follows Mechanism 1 with H<sub>2</sub>\* stabilized as the intermediate, while the reaction on Au, Ag, Ir, and Pt(111) follows Mechanism 2, which does not have an intermediate H<sub>2</sub>\* state. Our results on Cu are in reasonable agreement with the experimental observation by Svensson *et al.* using electron energy-loss measurements.<sup>65</sup> The overall energy barrier of hydrogen associative desorption (defined as the highest value of the free energy diagram of hydrogen desorption) follows the order: Au < Ir < Ag < Pt < Cu < Rh < Ni < Pd. The overall energy barriers of the surfaces with Mechanism 2 are higher than those with Mechanism 1. However, the presence of stabilized H<sub>2</sub>\* divides the process of hydrogen desorption into two elementary steps. For the surfaces with Mechanism 1 (Cu, Ni, Pd, and Rh), the formation of stabilized H<sub>2</sub>\* possesses a larger barrier than the H<sub>2</sub>\* desorption on Cu, Ni, and Pd, while the energy barriers of the two steps differ little on Rh.

We can also see what is special about Au, Ag, and Cu(111). The overall hydrogen desorption is an exothermic process on Au and Ag(111), while it is an endothermic process on Cu(111). Additionally, Au, Ag, and Cu(111) have higher energy barriers for the backward reaction, while other monometallics have relatively small energy barriers for this backward step.

Here, we discuss the origin of the two different mechanisms on these surfaces. Figure 4 shows the calculated PDOS of gas-phase H<sub>2</sub> and the d-electrons of a surface atom on the monometallic (111) surfaces. The main peaks of the d-electrons of Au, Ag, and Cu(111) are much lower than their Fermi level. Therefore, it is difficult for these weak-binding metals to donate electrons to the gas-phase H<sub>2</sub>, which leads to weak adsorption of H<sub>2</sub>. This is also why Au, Ag, and Cu have

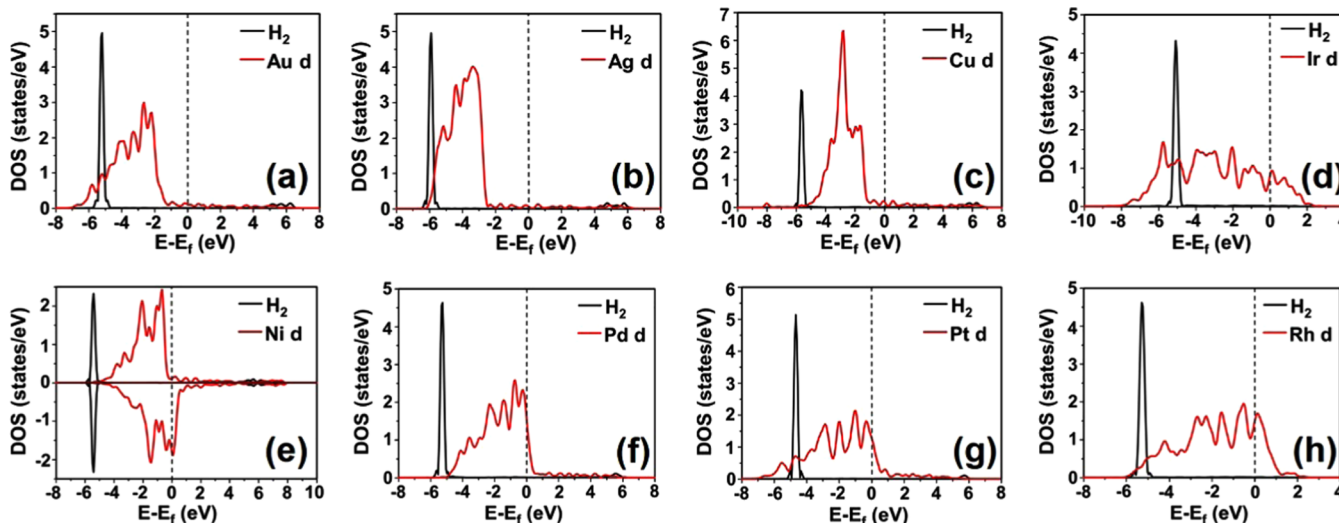


**Figure 4.** PDOS of gas-phase H<sub>2</sub> and metal d-orbital. (a) Au, (b) Ag, (c) Cu, (d) Ir, (e) Ni, (f) Pd, (g) Pt, and (h) Rh(111).

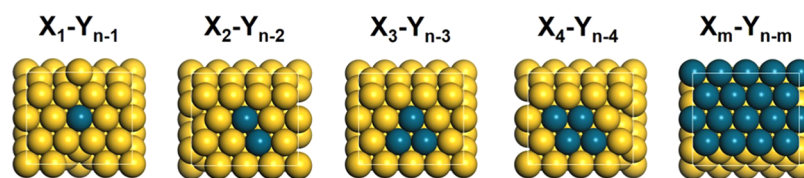


**Figure 5.** Configurations of bimetallic surfaces ( $X = \text{Ir, Ni, Pd, Pt, and Rh}$ ;  $Y = \text{Au, Ag, and Cu}$ ) are considered in this study. Yellow and deep green spheres represent  $Y$  and  $X$  elements, respectively.

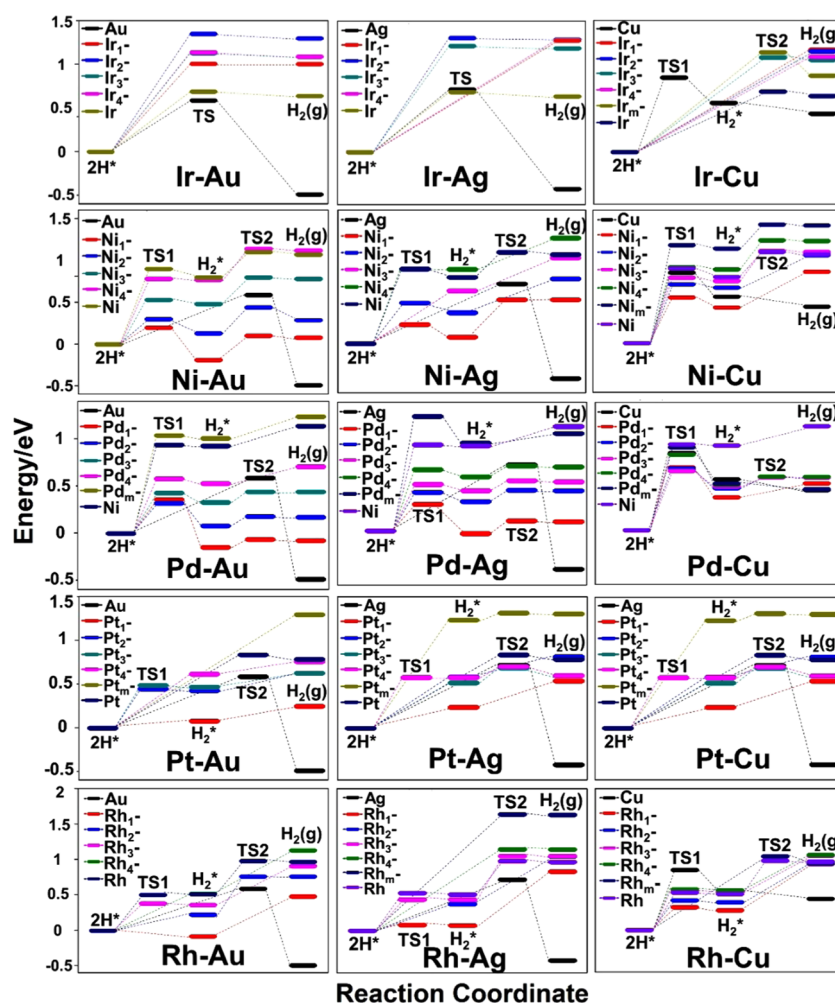


**Figure 6.** Free energy diagrams of hydrogen desorption on mono- and bimetallic (111) surfaces.

relatively high energy barriers for  $\text{H}_2$  dissociation. However, the overlap between the d-orbitals of Au/Ag and the s-orbital of  $\text{H}_2$  is more significant (Figure 4a,b) as compared to Cu (Figure 4c). Since a more significant overlap between the H atomic orbitals and the metal surface results in stronger bonding,<sup>66</sup>  $\text{H}_2$  on Au and Ag(111) tends to dissociate and form stable M–H bonds, while  $\text{H}_2$  is first stabilized on Cu(111).

For Ir, Ni, Pd, Pt, and Rh(111), their main d-orbital peaks all cross the Fermi level, which indicates that they can easily donate electrons for  $\text{H}_2$  adsorption and dissociation. This is why Ir, Ni, Pd, Pt, and Rh(111) have lower energy barriers for  $\text{H}_2$  dissociation compared to Au, Ag, and Cu(111). The overlap between the d-orbitals of Ir/Pt vs the s-orbital of  $\text{H}_2$  is significant (Figure 4d,g), while it is less significant on Ni/Pd/Rh (Figure 4e,f,h). Therefore,  $\text{H}_2$  on Ir and Pt(111) favors

dissociation (forming stable M–H bonds), while it forms a stabilized  $\text{H}_2^*$  on Ni, Pd, and Rh(111).

**3.2. Hydrogen Desorption on Bimetallic Alloy Surfaces.** We then analyzed hydrogen desorption on bimetallic X–Y ( $X = \text{Ir, Ni, Pd, Pt, and Rh}$ ;  $Y = \text{Au, Ag, and Cu}$ ) (111) surfaces (with the bimetallic models shown in Figure 5 and hydrogen desorption pathways shown in Figures S2–S16). Figure 6 shows that Ir–Au, Ir–Ag, and Ir–Cu demonstrate a different hydrogen desorption chemistry from others. The hydrogen desorption on Ir–Au, Ir–Ag, and Ir–Cu surfaces follows Mechanism 2, similar to monometallic Ir(111). The energy barriers and the final state energies of hydrogen associative desorption are all higher on the Ir–Au, Ir–Ag, and Ir–Cu alloy surfaces, compared to those on Ir, Au, Ag, and Cu(111). In contrast, on the Ni–, Pd–, Pt–, and Rh–Au/Ag/Cu alloy surfaces, hydrogen desorption follows Mechanism 1 (except for  $\text{Pt}_m\text{-Au}_x$ ,  $\text{Pt}_m\text{-Cu}_x$ ,  $\text{Rh}_4\text{-Ag}_x$ ,

**Table 1. Summary of the Mechanism, Activation Energy Barrier ( $E_a$ ), Reaction Energy ( $E_R$ ), and Highest-Barrier Step [Value 1:  $2H^* \rightarrow H_2^*$ ; Value 2:  $H_2^* \rightarrow H_2$  (g).] of Hydrogen Associative Desorption on Mono- and Bimetallic (111) Surfaces**

	mechanism	$E_{a1}$ (eV)	$E_{R1}$ (eV)	$E_{a2}$ (eV)	$E_{R2}$ (eV)	highest-barrier step
Ir	2			0.69	0.64	
Ir <sub>1</sub> -Au <sub>x</sub>	2			1.01	1.00	
Ir <sub>2</sub> -Au <sub>x</sub>	2			1.35	1.30	
Ir <sub>3</sub> -Au <sub>x</sub>	2			1.13	1.09	
Ir <sub>4</sub> -Au <sub>x</sub>	2			1.14	1.09	
Ir <sub>1</sub> -Au <sub>x</sub>	2				1.28	
Ir <sub>2</sub> -Au <sub>x</sub>	2			1.31	1.29	
Ir <sub>3</sub> -Au <sub>x</sub>	2			1.22	1.19	
Ir <sub>4</sub> -Au <sub>x</sub>	2				1.28	
Ir <sub>1</sub> -Cu <sub>x</sub>	2				1.17	
Ir <sub>2</sub> -Cu <sub>x</sub>	2				1.15	
Ir <sub>3</sub> -Cu <sub>x</sub>	2			1.08	1.05	
Ir <sub>4</sub> -Cu <sub>x</sub>	2				1.09	
Ir <sub>m</sub> -Cu <sub>x</sub>	2			1.14	0.87	
Ni	1	0.90	0.80	0.30	0.27	1
Ni <sub>1</sub> -Au <sub>x</sub>	1	0.20	-0.19	0.29	0.27	2
Ni <sub>2</sub> -Au <sub>x</sub>	1	0.30	0.13	0.31	0.16	2
Ni <sub>3</sub> -Au <sub>x</sub>	1	0.53	0.48	0.32	0.30	1
Ni <sub>4</sub> -Au <sub>x</sub>	1	0.78	0.77	0.37	0.35	1
Ni <sub>1</sub> -Ag <sub>x</sub>	1	0.23	0.08	0.45	0.44	2
Ni <sub>2</sub> -Ag <sub>x</sub>	1	0.49	0.37		0.41	1
Ni <sub>3</sub> -Ag <sub>x</sub>	1	0.64	0.63		0.40	1
Ni <sub>4</sub> -Ag <sub>x</sub>	1	0.90	0.89		0.37	1
Ni <sub>1</sub> -Cu <sub>x</sub>	1	0.55	0.43		0.43	1
Ni <sub>2</sub> -Cu <sub>x</sub>	1	0.71	0.67		0.39	1
Ni <sub>3</sub> -Cu <sub>x</sub>	1	0.79	0.75	0.36	0.35	1
Ni <sub>4</sub> -Cu <sub>x</sub>	1	0.92	0.89	0.35	0.34	1
Ni <sub>m</sub> -Cu <sub>x</sub>	1	1.18	1.14	0.29	0.28	1
Pd	1	0.94	0.93		0.21	1
Pd <sub>1</sub> -Au <sub>x</sub>	1	0.36	-0.15	0.084	0.071	1
Pd <sub>2</sub> -Au <sub>x</sub>	1	0.32	0.08	0.10	0.09	1
Pd <sub>3</sub> -Au <sub>x</sub>	1	0.43	0.33	0.12	0.11	1
Pd <sub>4</sub> -Au <sub>x</sub>	1	0.58	0.53		0.18	1
Pd <sub>m</sub> -Au <sub>x</sub>	1	1.04	1.01		0.23	1
Pd <sub>1</sub> -Ag <sub>x</sub>	1	0.29	-0.03	0.14	0.13	1
Pd <sub>2</sub> -Ag <sub>x</sub>	1	0.42	0.32	0.12	0.11	1
Pd <sub>3</sub> -Ag <sub>x</sub>	1	0.51	0.44	0.11	0.10	1
Pd <sub>4</sub> -Ag <sub>x</sub>	1	0.67	0.59	0.12	0.11	1
Pd <sub>m</sub> -Ag <sub>x</sub>	1	1.25	0.96		0.10	1
Pd <sub>1</sub> -Cu <sub>x</sub>	1	0.69	0.36		0.15	1
Pd <sub>2</sub> -Cu <sub>x</sub>	1	0.68	0.46	0.13	0.12	1
Pd <sub>3</sub> -Cu <sub>x</sub>	1	0.65	0.48	0.10	0.09	1
Pd <sub>4</sub> -Cu <sub>x</sub>	1	0.83	0.50	0.09	0.08	1
Pd <sub>m</sub> -Cu <sub>x</sub>	1	0.91	0.51		-0.06	1
Pt	2			0.84	0.79	
Pt <sub>1</sub> -Au <sub>x</sub>	1		0.08		0.17	2
Pt <sub>2</sub> -Au <sub>x</sub>	1	0.45	0.43		0.20	1
Pt <sub>3</sub> -Au <sub>x</sub>	1	0.49	0.47		0.16	1
Pt <sub>4</sub> -Au <sub>x</sub>	1		0.62		0.14	1
Pt <sub>m</sub> -Au <sub>x</sub>	2				1.30	
Pt <sub>1</sub> -Ag <sub>x</sub>	1		0.24		0.30	2
Pt <sub>2</sub> -Ag <sub>x</sub>	1		0.59		0.23	1
Pt <sub>3</sub> -Ag <sub>x</sub>	1		0.52	0.17	0.08	1
Pt <sub>4</sub> -Ag <sub>x</sub>	1	0.59	0.58	0.12	0.02	1
Pt <sub>m</sub> -Ag <sub>x</sub>	1		1.24	0.08	0.07	1
Pt <sub>1</sub> -Cu <sub>x</sub>	1	0.39	0.38		0.25	1
Pt <sub>2</sub> -Cu <sub>x</sub>	1	0.42	0.41		0.18	1
Pt <sub>3</sub> -Cu <sub>x</sub>	1	0.46	0.44	0.12	0.11	1
Pt <sub>4</sub> -Cu <sub>x</sub>	1	0.50	0.47	0.07	-0.01	1
Pt <sub>m</sub> -Cu <sub>x</sub>	2			0.86	0.47	

Table 1. continued

	mechanism	$E_{a1}$ (eV)	$E_{R1}$ (eV)	$E_{a2}$ (eV)	$E_{R2}$ (eV)	highest-barrier step
Rh	1	0.53	0.51	0.47	0.46	1
Rh <sub>1</sub> -Au <sub>x</sub>	1		-0.084		0.56	2
Rh <sub>2</sub> -Au <sub>x</sub>	1		0.22	0.55	0.54	2
Rh <sub>3</sub> -Au <sub>x</sub>	1	0.38	0.36		0.55	2
Rh <sub>4</sub> -Au <sub>x</sub>	1		0.52		0.61	2
Rh <sub>1</sub> -Ag <sub>x</sub>	1	0.076	0.072		0.76	2
Rh <sub>2</sub> -Ag <sub>x</sub>	1		0.38		0.67	2
Rh <sub>3</sub> -Ag <sub>x</sub>	1	0.44	0.43	0.62	0.61	2
Rh <sub>4</sub> -Ag <sub>x</sub>	2			1.15	1.14	
Rh <sub>m</sub> -Ag <sub>x</sub>	2			1.64	1.63	
Rh <sub>1</sub> -Cu <sub>x</sub>	1	0.32	0.28		0.66	2
Rh <sub>2</sub> -Cu <sub>x</sub>	1	0.42	0.39		0.55	2
Rh <sub>3</sub> -Cu <sub>x</sub>	1	0.56	0.53		0.52	1
Rh <sub>4</sub> -Cu <sub>x</sub>	1	0.58	0.56		0.50	1
Rh <sub>m</sub> -Cu <sub>x</sub>	2			1.05	0.95	
Au	2			0.59	-0.49	
Ag	2			0.72	-0.42	
Cu	1	0.85	0.56		-0.12	1

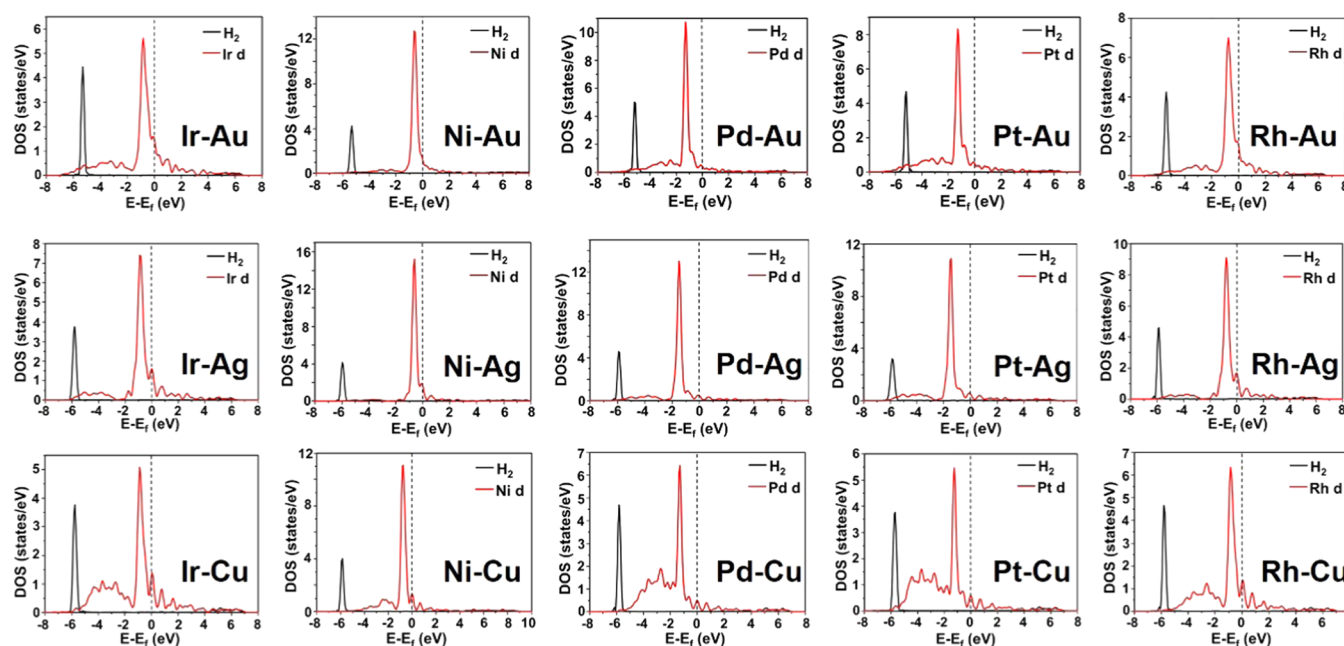


Figure 7. PDOSs for gas-phase H<sub>2</sub> and the d-orbital of an X atom on each X<sub>1</sub>-Y<sub>n-1</sub> bimetallic alloy (111) (X = Ir, Ni, Pd, Pt, and Rh; Y = Au, Ag, and Cu).

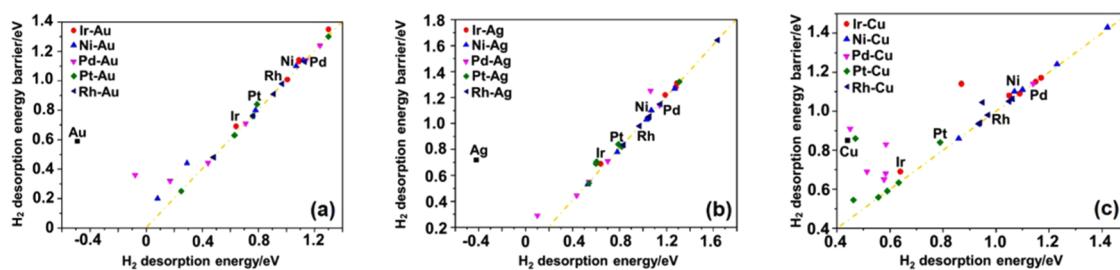
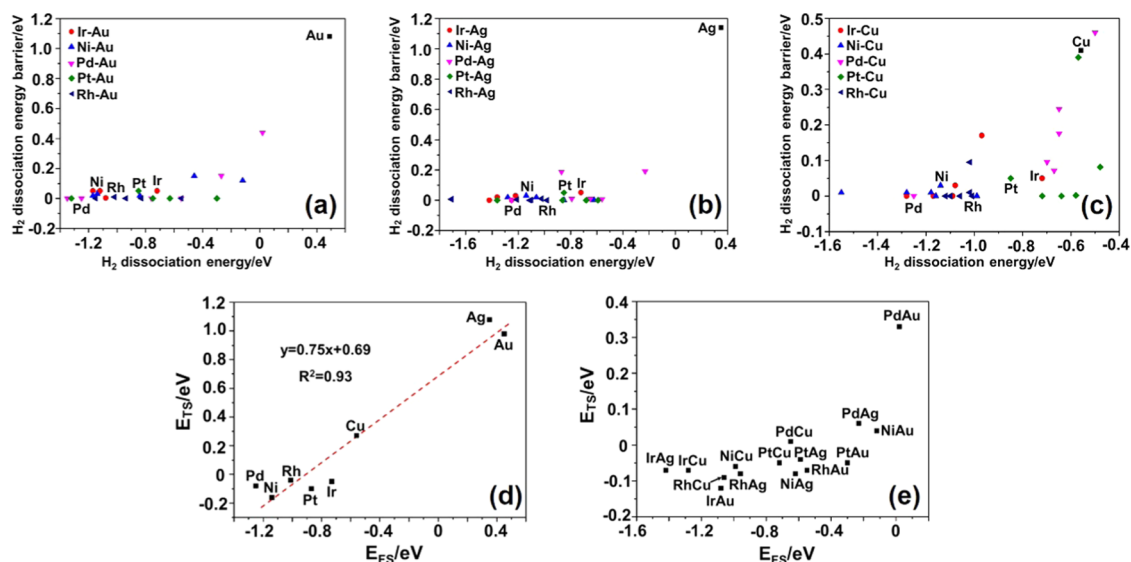


Figure 8. Hydrogen desorption energy barrier as a function of hydrogen desorption energy. (a) X-Au, (b) X-Ag, and (c) X-Cu (X = Ir, Ni, Pd, Pt, and Rh) alloy (111) surfaces and monometallic surfaces.

Rh<sub>m</sub>-Ag<sub>x</sub> and Rh<sub>m</sub>-Cu<sub>x</sub>). Ir-, Ni-, Pd- and Rh-Au/Ag/Cu follow the same mechanism as monometallics Ir, Ni, Pd, and Rh. However, hydrogen desorption on most ensembles on the

Pt-Au/Ag/Cu alloy surfaces follows Mechanism 1 (except for Pt<sub>m</sub>-Au and Pt<sub>m</sub>-Cu<sub>x</sub>), while it follows Mechanism 2 on Pt(111).



**Figure 9.**  $H_2$  adsorption energy barrier ( $E_{TS}$ ) vs  $H_2$  adsorption energy ( $E_{FS}$ ) on (a) X–Au, (b) X–Ag, (c) X–Cu (X = Ir, Ni, Pd, Pt, and Rh) alloy and monometallic surfaces and (d) monometallic and (e) single-atom doped alloy [ $X_1$ –Au, –Ag, and –Cu (X = Ir, Ni, Pd, Pt, and Rh)] surfaces.  $E_{FS}$  is the energy of the final state of  $H_2$  dissociative adsorption, relative to the gas-phase species and a clean surface.  $E_{TS}$  is the energy of the transition state with the same reference.

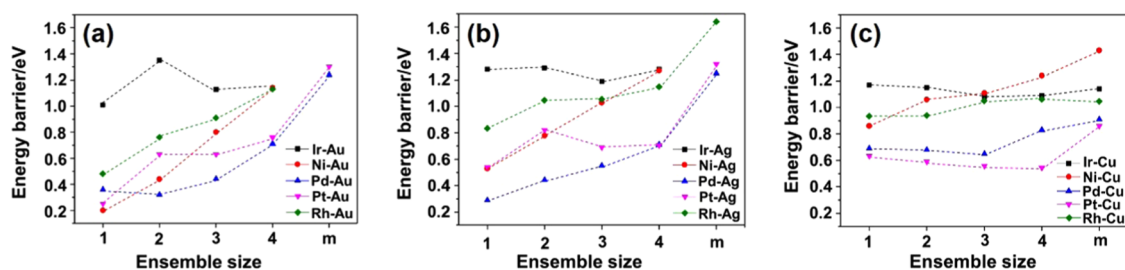


**Figure 10.** Hydrogen desorption energy barrier vs ensemble size (1, 2, 3, 4, and monolayer). (a) X–Au, (b) X–Ag, and (c) X–Cu (X = Ir, Ni, Pd, Pt, and Rh) (111) surfaces.

Notably, it can be seen that the energy barriers of hydrogen desorption are lower on the small ensembles of Ni–, Pd–, Pt–, Rh–Au/Ag, and Pd– and Pt–Cu, compared to their monometallic counterparts. The energy barriers of hydrogen desorption increase with the ensemble size on most of the Au/Ag-based alloys and Ni–Cu alloys. For Ni–Au, Pt–Au, Pt–Ag, and Rh–Cu, which follow Mechanism 1, the highest-barrier step varies with different ensemble sizes, as shown in Table 1.

Figure 7 shows the PDOSs of gas-phase  $H_2$  and the d-orbital of an X atom on the  $X_1$ – $Y_{n-1}$  alloy surfaces (X = Ir, Ni, Pd, Pt, and Rh; Y = Au, Ag, and Cu). The X atoms generally have very high and sharp peaks near the Fermi level, which indicates that it is easy to donate electrons to  $H_2$ . Compared to the broader bands of monometallics, the sharp peaks of alloys suggest that electrons are localized by the combination of two metals, resulting in a reduced overlap between X-d and the  $H_2$ -s (except for those of Ir–Au/Ag/Cu). Because of the large d-orbital of Ir, there is still a broad Ir band at energies lower than the sharp peak after alloying. Therefore, the overlap between the d-orbitals of Ir and the s-orbitals of  $H_2$  on Ir<sub>1</sub>–Au/Ag/Cu is still significant. This is why hydrogen desorption on Ir–Au/Ag/Cu alloys follows Mechanism 2, as on pure Ir. The hydrogen associative desorption on other alloys (Ni–, Pd–, Pt–, and Rh–Au/Ag/Cu) follows Mechanism 1 since there is little overlap between the d-orbitals of X atoms and  $H_2$ -s (Figures S17–S31).

Figure 8 shows the correlation between the hydrogen desorption energy barrier and the hydrogen desorption energy on X–Y alloy surfaces (X = Ir, Ni, Pd, Pt, and Rh; Y = Au, Ag, and Cu). The overall energy barrier is defined as the hydrogen desorption barrier, and the energy difference between the initial and final states is the hydrogen desorption energy. Hydrogen desorption on most of the bimetallic alloys and monometallics follows the linear Brønsted–Evans–Polanyi (BEP) relationship,<sup>67</sup> with the exception of monometallics Au, Ag, Cu, Pd<sub>1,2</sub>–Au<sub>x</sub>, Ni<sub>1,2</sub>–Au<sub>x</sub>, Pd<sub>1,m</sub>–Ag<sub>x</sub>, Ir<sub>m</sub>–Cu<sub>x</sub>, Pt<sub>m</sub>–Cu<sub>x</sub>, and Pd–Cu. As shown in Figure 4a–c, the energy levels of the d-orbitals of Au, Ag, and Cu are much lower than the Fermi level, leading to low electron donation to  $H_2$ . Similarly, the energy levels of the d-orbitals of these alloys are lower than their monometallic counterparts and other alloys shown in Figures S17–S31. Therefore, they are less able to donate electrons to  $H_2$ . Figure 6 provides the same result that gas-phase  $H_2$  on those alloys has to overcome a high barrier to form two co-adsorbed  $H^*$  atoms, resulting in a high barrier for the backward reaction as well. For other bimetallic alloys and monometallics, their hydrogen desorption energies and energy barriers differ by only a little, indicating that it is easy to adsorb or dissociate the gas-phase  $H_2$ . Therefore, correlations between the desorption energy barrier and the desorption energy on most of the mono- and bimetallic surfaces are linear with a slope close to unity.

**3.3. Hydrogen Dissociative Adsorption.** Next, we discuss the backward reaction ( $H_2$  dissociative adsorption) from gas-phase  $H_2$  to  $H_2^*$  and then to two co-adsorbed  $H^*$  atoms on mono- and bimetallic surfaces. Figure 9a–c shows that the  $H_2$  dissociative adsorption barriers on Au-, Ag-, Cu-based alloys and monometallics do not show a clear linear correlation with their corresponding reaction energies.

In contrast, on monometallic (111) surfaces, we can see that  $H_2$  adsorption follows a clear linear trend with  $R^2 = 0.93$  (Figure 9d). The  $H_2$  dissociative adsorption barriers on  $X_1$ -Au, -Ag, and -Cu alloys also have a near-monotonic trend with the reaction energy (Figure 9e). The trendline of these single-atom doped alloys is right-shifted compared to that of the monometallics. This is in good agreement with the previous study in ref 68. Similarly, as shown in Figure 6, the reaction energies of  $H_2$  adsorption on most of the alloys with Au/Ag/Cu-rich ensembles are higher than those on monometallics. The reaction energies on all Ir-based alloys are lower than those on pure Ir, Au, Ag, and Cu. Besides, Pd–Cu and Pt–Cu alloys show higher reaction energies, while other Cu-based alloys show lower values.

To find the most promising alloys for hydrogen desorption, we analyzed the relationship between the hydrogen associative desorption energy barrier and the ensemble size of the alloy elements (1, 2, 3, 4, and monolayer) (Figure 10). The hydrogen desorption energy barrier increases with the ensemble size on Au- and Ag-based alloys and Ni–Cu alloys (except for Ir-based alloys and  $Pt_2$ -Ag<sub>x</sub>). However, the hydrogen desorption energy on Cu- and Ir-based alloys is nearly independent of the ensemble size (except for Ni–Cu). The best alloys for hydrogen associative desorption are primarily single-atom alloys, with the exceptions of Ir–Ag, Ir–Cu, Pd–Cu, and Pt–Cu. The most promising alloys for hydrogen associative desorption are  $Ni_{11}, Ni_2-Au_x, Ni_1-Ag_x, Pd_1, Pd_2, Pd_3-Au_x, Pd_1, Pd_2, Pd_3-Ag_x, Pt_1-Au_x, Pt_1-Ag_x, Pt_3, Pt_4-Cu_x,$  and  $Rh_1-Au_x$  with energy barriers lower than any monometallic (Au, 0.59 eV). The overall trend of the hydrogen associative desorption barriers is  $Pd < Pt < Ni < Rh < Ir$  for Au- and Ag-based alloys and  $Pt < Pd < Rh < Ir < Ni$  for Cu-based alloys, which is much different from the order of their monometallic counterparts ( $Ir < Pt < Rh < Ni < Pd$ ).

## 4. CONCLUSIONS

We have analyzed the trends of hydrogen desorption on 8 monometallic and 70 bimetallic close-packed surfaces and identified two different mechanisms for the hydrogen desorption, either to an adsorbed  $H_2$  species or to gas-phase  $H_2$ . The selectivity toward the two mechanisms can be explained by the different magnitudes of the PDOS overlap between the gas-phase  $H_2$  orbitals and the d-orbitals of atoms on the metal surface. A linear BEP relationship was found on both the mono- and bimetallic surfaces, which suggests that we can predict the  $H_2$  desorption kinetics based on their binding energies with minimal computation cost. Finally, our results indicate that most of the bimetallic alloy surfaces with Au/Ag/Cu-rich ensembles can effectively reduce the energy barriers of hydrogen associative desorption. We expect that this study will provide helpful guidelines for the design of high-performance hydrogen storage materials, hydrogen fuel cells, and organic molecule reforming catalysts.

## ■ ASSOCIATED CONTENT

### Supporting Information

The Supporting Information is available free of charge at <https://pubs.acs.org/doi/10.1021/acs.jpcc.1c03466>.

Comparison of desorption energies and mechanisms on Pt and Pt–Au surfaces by different methods; hydrogen desorption pathways on the monometallic and bimetallic surfaces; and PDOS of gas-phase  $H_2$  and the d-orbital of a transition-metal atom on a Au/Ag/Cu surface (PDF)

## ■ AUTHOR INFORMATION

### Corresponding Authors

**Zhen Zhao** – State Key Laboratory of Heavy Oil Processing, College of Science, China University of Petroleum-Beijing, Beijing 102249, China; Institute of Catalysis for Energy and Environment, Shenyang Normal University, Shenyang 110034, China; [orcid.org/0000-0003-0044-5512](https://orcid.org/0000-0003-0044-5512); Email: [zhenzhao@cup.edu.cn](mailto:zhenzhao@cup.edu.cn)

**Graeme Henkelman** – Department of Chemistry and the Oden Institute for Computational Engineering and Sciences, University of Texas at Austin, Austin, Texas 78712-0231, United States; [orcid.org/0000-0002-0336-7153](https://orcid.org/0000-0002-0336-7153); Email: [henkelman@utexas.edu](mailto:henkelman@utexas.edu)

### Authors

**Huiling Zheng** – State Key Laboratory of Heavy Oil Processing, College of Science, China University of Petroleum-Beijing, Beijing 102249, China; Department of Chemistry and the Oden Institute for Computational Engineering and Sciences, University of Texas at Austin, Austin, Texas 78712-0231, United States; [orcid.org/0000-0001-8347-3724](https://orcid.org/0000-0001-8347-3724)

**Hao Li** – Department of Chemistry and the Oden Institute for Computational Engineering and Sciences, University of Texas at Austin, Austin, Texas 78712-0231, United States; Present Address: Department of Physics, Technical University of Denmark, 2800 Kongens Lyngby, Denmark; [orcid.org/0000-0002-7577-1366](https://orcid.org/0000-0002-7577-1366)

**Weiyu Song** – State Key Laboratory of Heavy Oil Processing, College of Science, China University of Petroleum-Beijing, Beijing 102249, China; [orcid.org/0000-0001-5720-204X](https://orcid.org/0000-0001-5720-204X)

Complete contact information is available at:

<https://pubs.acs.org/doi/10.1021/acs.jpcc.1c03466>

### Author Contributions

<sup>||</sup>H.Z. and H.L. contributed equally to this work.

### Notes

The authors declare no competing financial interest.

## ■ ACKNOWLEDGMENTS

The authors are grateful for financial support from the National Natural Science Foundation of China (91845201 and U1908204) and the China Scholarship Council (201806440058). The work at UT Austin was supported by the Welch Foundation (F-1841) and the Texas Advanced Computing Center.

## ■ REFERENCES

(1) Pfeffer, M. Selected Applications to Organic Synthesis of Intramolecular C–H Activation Reactions by Transition Metals. *Pure Appl. Chem.* **1992**, *64*, 335–342.

- (2) Blomberg, M. R.; Siegbahn, P. E.; Nagashima, U.; Wennerberg, J. Theoretical Study of the Activation of C-C Bonds by Transition Metal Atoms. *J. Am. Chem. Soc.* **1991**, *113*, 424–433.
- (3) Liao, M. S.; Au, C. T.; Ng, C. F. Methane Dissociation on Ni, Pd, Pt and Cu Metal (111) Surfaces - A Theoretical Comparative Study. *Chem. Phys. Lett.* **1997**, *272*, 445–452.
- (4) Ji, Y.; Li, W.; Xu, H.; Chen, Y. A Study of Carbon Deposition on Catalysts during the Catalytic Partial Oxidation of Methane to Syngas in Fluidized Bed Reactor. *React. Kinet. Catal. Lett.* **2001**, *73*, 27–32.
- (5) Zhang, R.; Song, L.; Wang, Y. Insight into the Adsorption and Dissociation of CH<sub>4</sub> on Pt (h k l) Surfaces: A Theoretical Study. *Appl. Surf. Sci.* **2012**, *258*, 7154–7160.
- (6) German, E. D.; Sheintuch, M. Predicting CH<sub>4</sub> Dissociation Kinetics on Metals: Trends, Sticking Coefficients, H Tunneling, and Kinetic Isotope Effect. *J. Phys. Chem. C* **2013**, *117*, 22811–22826.
- (7) Wang, B.; Song, L.; Zhang, R. The Dehydrogenation of CH<sub>4</sub> on Rh(111), Rh(110) and Rh(100) Surfaces: A Density Functional Theory Study. *Appl. Surf. Sci.* **2012**, *258*, 3714–3722.
- (8) Rezaei, M.; Alavi, S. M.; Sahebdehfar, S.; Yan, Z. F. Syngas Production by Methane Reforming with Carbon Dioxide on Noble Metal Catalysts. *J. Nat. Gas Chem.* **2006**, *15*, 327–334.
- (9) Fierro, V.; Klouz, V.; Akdim, O.; Mirodatos, C. Oxidative Reforming of Biomass Derived Ethanol for Hydrogen Production in Fuel Cell Applications. *Catal. Today* **2002**, *75*, 141–144.
- (10) Evans, E. J.; Li, H.; Yu, W. Y.; Mullen, G. M.; Henkelman, G.; Mullins, C. B. Mechanistic Insights on Ethanol Dehydrogenation on Pd-Au Model Catalysts: A Combined Experimental and DFT Study. *Phys. Chem. Chem. Phys.* **2017**, *19*, 30578–30589.
- (11) Vaidya, P. D.; Rodrigues, A. E. Glycerol Reforming for Hydrogen Production: A Review. *Chem. Eng. Technol.* **2009**, *32*, 1463–1469.
- (12) Contreras, J. L.; Salmones, J.; Colín-Luna, J. A.; Nuño, L.; Quintana, B.; Córdova, I.; Zeifert, B.; Tapia, C.; Fuentes, G. A. Catalysts for H<sub>2</sub> Production Using the Ethanol Steam Reforming (A Review). *Int. J. Hydrogen Energy* **2014**, *39*, 18835–18853.
- (13) Liu, H.; Zhang, R.; Yan, R.; Li, J.; Wang, B.; Xie, K. Insight into CH<sub>4</sub> Dissociation on NiCu Catalyst: A First-Principles Study. *Appl. Surf. Sci.* **2012**, *258*, 8177–8184.
- (14) Zuo, Z.; Huang, W.; Han, P.; Li, Z. A Density Functional Theory Study of CH<sub>4</sub> Dehydrogenation on Co(111). *Appl. Surf. Sci.* **2010**, *256*, 5929–5934.
- (15) Wang, Z.; Cao, X. M.; Zhu, J.; Hu, P. Activity and Coke Formation of Nickel and Nickel Carbide in Dry Reforming: A Deactivation Scheme from Density Functional Theory. *J. Catal.* **2014**, *311*, 469–480.
- (16) Roy, S.; Hariharan, S.; Tiwari, A. K. Pt-Ni Subsurface Alloy Catalysts: An Improved Performance toward CH<sub>4</sub> Dissociation. *J. Phys. Chem. C* **2018**, *122*, 10857–10870.
- (17) Liu, S.; Guan, L.; Li, J.; Zhao, N.; Wei, W.; Sun, Y. CO<sub>2</sub> Reforming of CH<sub>4</sub> over Stabilized Mesoporous Ni-CaO-ZrO<sub>2</sub> Composites. *Fuel* **2008**, *87*, 2477–2481.
- (18) Ashcroft, A. T.; Cheetham, A.; Green, M.; Vernon, P. D. F. Partial Oxidation of Methane to Synthesis Gas Using Carbon Dioxide. *Nature* **1991**, *352*, 225–226.
- (19) Bradford, M. C. J.; Vannice, M. A. CO<sub>2</sub> Reforming of CH<sub>4</sub>. *Catal. Rev.* **1999**, *41*, 1–42.
- (20) Alcalá, R.; Mavrikakis, M.; Dumesic, J. A. DFT Studies for Cleavage of C-C and C-O Bonds in Surface Species Derived from Ethanol on Pt(111). *J. Catal.* **2003**, *218*, 178–190.
- (21) Li, H.; Evans, E. J., Jr; Mullins, C. B.; Henkelman, G. Ethanol Decomposition on Pd-Au Alloy Catalysts. *J. Phys. Chem. C* **2018**, *122*, 22024–22032.
- (22) Li, H.; Chai, W.; Henkelman, G. Selectivity for Ethanol Partial Oxidation: The Unique Chemistry of Single-Atom Alloy Catalysts on Au, Ag, and Cu(111). *J. Mater. Chem. A* **2019**, *7*, 23868–23877.
- (23) Taft, C. A.; Guimaraes, T. C.; Pavao, A. C.; Lester, W. A., Jr Adsorption and Dissociation of Diatomic Molecules on Transition-Metal Surfaces. *Int. Rev. Phys. Chem.* **1999**, *18*, 163–233.
- (24) Gudmundsdóttir, S.; Skúlason, E.; Weststrate, K. J.; Juurlink, L.; Jónsson, H. Hydrogen Adsorption and Desorption at the Pt(110)-(1×2) Surface: Experimental and Theoretical Study. *Phys. Chem. Chem. Phys.* **2013**, *15*, 6323–6332.
- (25) Olander, D. R.; Ullman, A. Analysis of Nonlinear Reactions in Modulated Molecular Beam Surface Experiments. *Int. J. Chem. Kinet.* **1976**, *8*, 625–637.
- (26) Denzler, D. N.; Frischkorn, C.; Wolf, M.; Ertl, G. Surface Femtochemistry: Associative Desorption of Hydrogen from Ru(001) Induced by Electronic Excitations. *J. Phys. Chem. B* **2004**, *108*, 14503–14510.
- (27) Khanuja, M.; Kala, S.; Mehta, B. R.; Kruis, F. E. Concentration-Specific Hydrogen Sensing Behavior in Monosized Pd Nanoparticle Layers. *Nanotechnology* **2009**, *20*, No. 015502.
- (28) Johansson, M.; Lytken, O.; Chorkendorff, I. The Sticking Probability for H<sub>2</sub> on Some Transition Metals at a Hydrogen Pressure of 1 Bar. *J. Chem. Phys.* **2008**, *128*, No. 034706.
- (29) Besenbacher, F.; Chorkendorff, I.; Clausen, B. S.; Hammer, B.; Molenbroek, A. M.; Nørskov, J. K.; Stensgaard, I. Design of a Surface Alloy Catalyst for Steam Reforming. *Science* **1998**, *279*, 1913–1915.
- (30) Bengaard, H. S.; Nørskov, J. K.; Sehested, J.; Clausen, B. S.; Nielsen, L. P.; Molenbroek, A. M.; Rostrup-Nielsen, J. R. Steam Reforming and Graphite Formation on Ni Catalysts. *J. Catal.* **2002**, *209*, 365–384.
- (31) Xu, Y.; Fan, C.; Zhu, Y. A.; Li, P.; Zhou, X. G.; Chen, D.; Yuan, W. K. Effect of Ag on the Control of Ni-catalyzed Carbon Formation: A Density Functional Theory Study. *Catal. Today* **2012**, *186*, 54–62.
- (32) Özkara-Aydinoğlu, Ş.; Aksoylu, A. E. CO<sub>2</sub> Reforming of Methane over Pt-Ni/Al<sub>2</sub>O<sub>3</sub> Catalysts: Effects of Catalyst Composition, and Water and Oxygen Addition to the Feed. *Int. J. Hydrogen Energy* **2011**, *36*, 2950–2959.
- (33) Menegazzo, F.; Signoretto, M.; Pinna, F.; Canton, P.; Pernicone, N. Optimization of Bimetallic Dry Reforming Catalysts by Temperature Programmed Reaction. *Appl. Catal., A* **2012**, *439–440*, 80–87.
- (34) Roy, S.; Hariharan, S.; Tiwari, A. K. Pt-Ni Subsurface Alloy Catalysts: An Improved Performance toward CH<sub>4</sub> Dissociation. *J. Phys. Chem. C* **2018**, *122*, 10857–10870.
- (35) Li, K.; Jiao, M.; Wang, Y.; Wu, Z. CH<sub>4</sub> Dissociation on NiM(111) (M = Co, Rh, Ir) Surface: A First-Principles Study. *Surf. Sci.* **2013**, *617*, 149–155.
- (36) Zhu, L. D.; Zhao, T. S.; Xu, J. B.; Liang, Z. X. Preparation and Characterization of Carbon-Supported Sub-Monolayer Palladium Decorated Gold Nanoparticles for the Electro-Oxidation of Ethanol in Alkaline Media. *J. Power Sources* **2009**, *187*, 80–84.
- (37) He, Q.; Chen, W.; Mukerjee, S.; Chen, S.; Laufek, F. Carbon-Supported PdM (M = Au and Sn) Nanocatalysts for the Electrooxidation of Ethanol in High pH Media. *J. Power Sources* **2009**, *187*, 298–304.
- (38) Xu, J. B.; Zhao, T. S.; Li, Y. S.; Yang, W. W. Synthesis and Characterization of the Au-Modified Pd Cathode Catalyst for Alkaline Direct Ethanol Fuel Cells. *Int. J. Hydrogen Energy* **2010**, *35*, 9693–9700.
- (39) Tedsree, K.; Li, T.; Jones, S.; Chan, C. W. A.; Yu, K. M. K.; Bagot, P. A.; Marquis, E. A.; Smith, G. D. W.; Tsang, S. C. E. Hydrogen Production from Formic Acid Decomposition at Room Temperature Using a Ag-Pd Core-Shell Nanocatalyst. *Nanotechnology* **2011**, *6*, 302–307.
- (40) Cho, J.; Lee, S.; Han, J.; Yoon, S. P.; Nam, S. W.; Choi, S. H.; Lee, K. Y.; Ham, H. C. Importance of Ligand Effect in Selective Hydrogen Formation via Formic Acid Decomposition on the Bimetallic Pd/Ag Catalyst from First-Principles. *J. Phys. Chem. C* **2014**, *118*, 22553–22560.
- (41) Li, H.; Shin, K.; Henkelman, G. Effects of Ensembles, Ligand, and Strain on Adsorbate Binding to Alloy Surfaces. *J. Chem. Phys.* **2018**, *149*, No. 174705.
- (42) Takehiro, N.; Liu, P.; Bergbreiter, A.; Nørskov, J. K.; Behm, R. J. Hydrogen Adsorption on Bimetallic PdAu(111) Surface Alloys: Minimum Adsorption Ensemble, Ligand and Ensemble Effects, and

Ensemble Confinement. *Phys. Chem. Chem. Phys.* **2014**, *16*, 23930–23943.

(43) Evans, E. J., Jr; Li, H.; Han, S.; Henkelman, G.; Mullins, C. B. Oxidative Cross-Esterification and Related Pathways of Co-Adsorbed Oxygen and Ethanol on Pd-Au. *ACS Catal.* **2019**, *9*, 4516–4525.

(44) Li, H.; Henkelman, G. Dehydrogenation Selectivity of Ethanol on Close-Packed Transition Metal Surfaces: A Computational Study of Monometallic, Pd/Au, and Rh/Au Catalysts. *J. Phys. Chem. C* **2017**, *121*, 27504–27510.

(45) Zhong, W.; Qi, Y.; Deng, M. The Ensemble Effect of Formic Acid Oxidation on Platinum-Gold Electrode Studied by First-Principles Calculations. *J. Power Sources* **2015**, *278*, 203–212.

(46) Au, C. T.; Ng, C. F.; Liao, M. S. Methane Dissociation and Syngas Formation on Ru, Os, Rh, Ir, Pd, Pt, Cu, Ag, and Au: A Theoretical Study. *J. Catal.* **1999**, *185*, 12–22.

(47) Chehab, F.; Kirstein, W.; Thieme, F. Hydrogen Desorption from Ni Sites on (110) Cu-Ni Surfaces. *Surf. Sci.* **1981**, *108*, L419–L423.

(48) Kresse, G.; Furthmüller, J. Effect of Er Doping on the Electronic Structure Optical Properties of ZnO. *Phys. Rev. B.* **1996**, *54*, 11169–11186.

(49) Kresse, G.; Furthmüller, J. Efficiency of Ab-Initio Total Energy Calculations for Metals and Semiconductors Using a Plane-Wave Basis Set. *Comput. Mater. Sci.* **1996**, *6*, 15–50.

(50) Perdew, J. P.; Burke, K.; Ernzerhof, M. Generalized Gradient Approximation Made Simple. *Phys. Rev. Lett.* **1996**, *77*, 3865–3868.

(51) Blöchl, P. E. Projector Augmented-Wave Method. *Phys. Rev. B* **1994**, *50*, 17953–17979.

(52) Morgan, B. J.; Watson, G. W. A Density Functional Theory + U Study of Oxygen Vacancy Formation at the (110), (100), (101), and (001) Surfaces of Rutile TiO<sub>2</sub>. *J. Phys. Chem. C* **2009**, *113*, 7322–7328.

(53) Henkelman, G.; Uberuaga, B. P.; Jónsson, H. Climbing Image Nudged Elastic Band Method for Finding Saddle Points and Minimum Energy Paths. *J. Chem. Phys.* **2000**, *113*, 9901–9904.

(54) Henkelman, G.; Jónsson, H. Improved Tangent Estimate in the Nudged Elastic Band Method for Finding Minimum Energy Paths and Saddle Points. *J. Chem. Phys.* **2000**, *113*, 9978–9985.

(55) García, S.; Zhang, L.; Piburn, G. W.; Henkelman, G.; Humphrey, S. M. Microwave Synthesis of Classically Immiscible Rhodium-Silver and Rhodium-Gold Alloy Nanoparticles: Highly Active Hydrogenation Catalysts. *ACS Nano* **2014**, *8*, 11512–11521.

(56) Hammer, B. H. L. B.; Hansen, L. B.; Nørskov, J. K. Improved Adsorption Energetics within Density-Functional Theory Using Revised Perdew-Burke-Ernzerhof Functionals. *Phys. Rev. B* **1999**, *59*, 7413–7421.

(57) Grimme, S. Semiempirical GGA-Type Density Functional Constructed with a Long-Range Dispersion Correction. *J. Comput. Chem.* **2006**, *27*, 1787–1799.

(58) Wellendorff, J.; Silbaugh, T. L.; Garcia-Pintos, D.; Nørskov, J. K.; Bligaard, T.; Studt, F.; Campbell, C. T. A Benchmark Database for Adsorption Bond Energies to Transition Metal Surfaces and Comparison to Selected DFT Functionals. *Surf. Sci.* **2015**, *640*, 36–44.

(59) Wellendorff, J.; Lundgaard, K. T.; Møgelhøj, A.; Petzold, V.; Landis, D. D.; Nørskov, J. K.; Bligaard, T.; Jacobsen, K. W. Density Functionals for Surface Science: Exchange-Correlation Model Development with Bayesian Error Estimation. *Phys. Rev. B* **2012**, *85*, No. 235149.

(60) Robota, H. J.; Vielhaber, W.; Lin, M. C.; Segner, J.; Ertl, G. Dynamics of Interaction of H<sub>2</sub> and D<sub>2</sub> with Ni(110) and Ni(111) Surfaces. *Surf. Sci.* **1985**, *155*, 101–120.

(61) Rendulic, K. D.; Winkler, A. Adsorption and Desorption Dynamics as Seen through Molecular Beam Techniques. *Surf. Sci.* **1994**, *299–300*, 261–276.

(62) Kristinsdóttir, L.; Skúlason, E. A Systematic DFT Study of Hydrogen Diffusion on Transition Metal Surfaces. *Surf. Sci.* **2012**, *606*, 1400–1404.

(63) Ferrin, P.; Kandoi, S.; Nilekar, A. U.; Mavrikakis, M. Hydrogen Adsorption, Absorption and Diffusion on and in Transition Metal Surfaces: A DFT Study. *Surf. Sci.* **2012**, *606*, 679–689.

(64) Li, H.; Yan, C.; Guo, H.; Shin, K.; Humphrey, S. M.; Werth, C. J.; Henkelman, G. Cu<sub>x</sub>Ir<sub>1-x</sub> Nanoalloy Catalysts Achieve near 100% Selectivity for Aqueous Nitrite Reduction to NH<sub>3</sub>. *ACS Catal.* **2020**, *10*, 7915–7921.

(65) Svensson, K.; Bengtsson, L.; Bellman, J.; Hassel, M.; Persson, M.; Andersson, S. Two-Dimensional Quantum Rotation of Adsorbed H<sub>2</sub>. *Phys. Rev. Lett.* **1999**, *83*, 124–127.

(66) Krapp, A.; Bickelhaupt, F. M.; Frenking, G. Orbital Overlap and Chemical Bonding. *Chem. - Eur. J.* **2006**, *12*, 9196–9216.

(67) Van Santen, R. A.; Neurock, M.; Shetty, S. G. Reactivity Theory of Transition-Metal Surfaces: A Brønsted-Evans-Polanyi Linear Activation Energy-Free-Energy Analysis. *Chem. Rev.* **2010**, *110*, 2005–2048.

(68) Darby, M. T.; Stamatakis, M.; Michaelides, A.; Sykes, E. C. H. Lonely Atoms with Special Gifts: Breaking Linear Scaling Relationships in Heterogeneous Catalysis with Single-Atom Alloys. *J. Phys. Chem. Lett.* **2018**, *9*, 5636–5646.